Kinematics and Workspace of a Spatial 3-DoF Manipulator with Anti-parallelogram joints

Vimalesh Muralidharan, Christine Chevallereau, Philippe Wenger

Kinematics and workspace of a spatial 3-DoF manipulator with anti-parallelogram joints

Vimalesh Muralidharan, Christine Chevallereau, and Philippe Wenger

Nantes Université, École Centrale Nantes, CNRS, LS2N, UMR 6004, F-44000 Nantes, France
{Vimalesh.Muralidharan, Christine.Chevallereau, Philippe.Wenger} @ls2n.fr

Abstract. This paper introduces a novel spatial serial manipulator composed of three anti-parallelogram (X) joints arranged in two perpendicular planes and separated by offsets. The position of a point on the terminal link is controlled through the three joint angles. The inverse kinematic problem is solved analytically by decomposing it into two planar sub-problems. It is shown that this problem admits up to thirty-two solutions, and an example with these many solutions is presented. The singularities of this manipulator are derived and interpreted geometrically. Finally, the workspace of this manipulator accounting for the joint limits of each X-joint is visualized.

Keywords: Anti-parallelogram joint, spatial manipulator, inverse kinematics, workspace

1 Introduction

Serial robot manipulators predominantly comprise revolute and prismatic joints [1]. There are very few instances of commercial manipulators that use other types of joints. For example, the parallelogram mechanism can be found in some industrial manipulators [2] and surgical manipulators requiring remote center of motion [3]. On the other hand, the anti-parallelogram mechanism (X-joint) has not yet entered the commercial domain. However, recent research indicates that it has an excellent potential to function as a joint in a manipulator. For instance, it has been used in a continuum manipulator in [4] and a bio-mimicking system inspired by a bird's neck in [5].

A comparative study showed that the X-joint is better than a revolute joint in terms of the range of movement and stiffness modulation when they are antagonistically actuated by cables [6]. Its moving instantaneous center of rotation will be more suitable for modeling the intervertebral motion in a biological system [7]. Such results have motivated the development of 2-DoF joints based on the X-joint for bio-mimicking manipulators [8],[9].

This work proposes to build a 3-DoF spatial manipulator by arranging the X-joints serially in different planes. The kinematics and workspace of this new manipulator, designated as 3-X, are studied in detail.

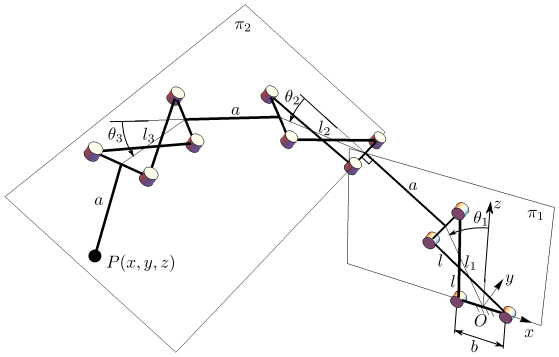

Fig. 1: Schematic of the spatial 3-X manipulator.

The rest of this paper is organized as follows: Section 2 describes the architecture of the 3-X manipulator. Section 3 presents its inverse kinematics. Section 4 studies the singularities of this manipulator, and section 5 plots its workspace. Finally, Section 6 presents the conclusions of this work.

2 Manipulator description

The kinematic diagram of the 3-X spatial manipulator at an arbitrary configuration is shown in Fig. 1. It comprises three identical planar X-joints, whose base and top bars are of length b while the crossed bars are of length l, with $(l > b)$ for its assembly. The first X-joint operates in the plane π_1, the xz-plane in the global frame of reference. On the other hand, the second and third joints operate in the plane π_2 that is perpendicular to π_1. There are 3 offsets of length a between successive joints and the last joint and the end-effector (EE) point P. The movement of joint i is measured by the coordinate θ_i, which is the orientation of the line joining the mid-points of the base and top bars of the X-joint relative to a reference perpendicular to its base. It is known that the orientation of the top-bar relative to the base is $2\theta_i$ for the X-joint [10]. Thus, it becomes possible to express the position of the EE of the manipulator using only the three joint angles $\theta_1, \theta_2, \theta_3$. From Fig. 1, the direct kinematics of the manipulator is presented as follows:

$$\begin{cases} x = -l_1(\theta_1)\sin\theta_1 - \sin(2\theta_1)\left\{a\cos(2(\theta_2+\theta_3)) + a\cos(2\theta_2) + a \right. \\ \qquad \left. + l_2(\theta_2)\cos\theta_2 + l_3(\theta_3)\cos(2\theta_2+\theta_3)\right\} \\ y = -l_2(\theta_2)\sin\theta_2 - a\sin(2(\theta_2+\theta_3)) - a\sin(2\theta_2) - l_3(\theta_3)\sin(2\theta_2+\theta_3) \\ z = l_1(\theta_1)\cos\theta_1 + \cos(2\theta_1)\left\{a\cos(2(\theta_2+\theta_3)) + a\cos(2\theta_2) + a \right. \\ \qquad \left. + l_3(\theta_3)\cos(2\theta_2+\theta_3) + l_2(\theta_2)\cos\theta_2\right\} \\ \text{where } l_i(\theta_i) = \sqrt{l^2 - b^2\cos^2\theta_i} \quad \text{for } i = 1,2,3 \end{cases} \tag{1}$$

3 Inverse kinematics

The inverse kinematics problem involves finding all possible joint angles $(\theta_1, \theta_2, \theta_3)$ for a given EE position (x, y, z). This problem can be decomposed into two planar sub-problems similar to that of a 3-R positioning manipulator whose first axis is perpendicular to the next two parallel axes [11], p. 76. The first sub-problem involves finding all possible θ_1 values, and the second sub-problem requires the computation of (θ_2, θ_3) for each value of θ_1. These problems are described in the next two sections, followed by a numerical example.

3.1 First sub-problem

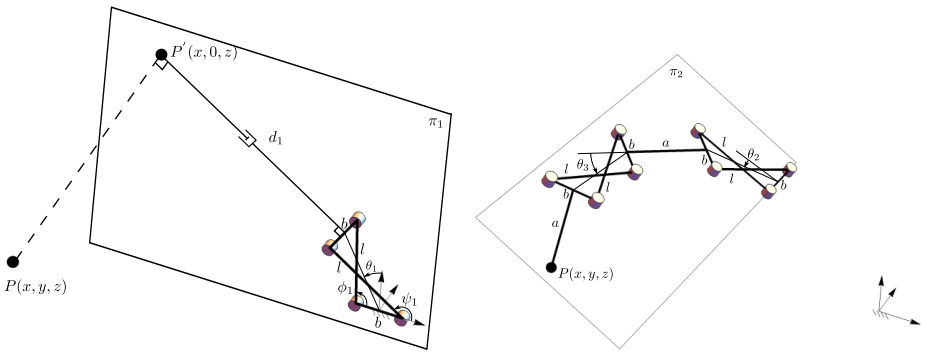

(a) Sub-problem 1 (b) Sub-problem 2

Fig. 2: Decomposition of the inverse kinematic problem of the 3-X manipulator.

Since the first X-joint is in plane π_1 that is perpendicular to the plane π_2 of the other two joints, it is possible to compute the feasible values of θ_1 independent of the other two angles. From Fig. 1, it is apparent that θ_1 cannot alter the y-coordinate of the point P. Hence, the given EE point can be projected on the plane π_1 to obtain the point $P^{'}(x, 0, z)$ as shown in Fig. 2a. The plane π_2 has been suppressed, but its line of intersection with π_1 is indicated by the segment connecting X-joint to the point $P^{'}$. A virtual prismatic joint with coordinate d_1 has been added along this line to locate the point $P^{'}$ from the first joint. Thus, we have an XP manipulator in the plane π_1.

The first sub-problem consists of finding all possible θ_1 that can position the plane π_2 to meet the point $P^{'}$ (or point P). Equivalently, it involves finding the feasible coordinates (θ_1, d_1) for a given point $P^{'}$.

It is possible to express the kinematics of this XP manipulator using $l_1 = \sqrt{l^2 - b^2 \cos^2 \theta_1}$ as in Eq. (1). However, the associated equations must be squared to eliminate the square roots, which would inject spurious solutions in the process. As an alternative, it is possible to express the direct kinematics in terms

of the intermediate angle (ϕ_1) and include the associated loop-closure equation in the model, as carried out in [10],[12]. This process leads to the following equations:

$$\begin{cases} -(b/2) + l\cos\phi_1 - (b/2)\cos(2\theta_1) - d_1\sin(2\theta_1) - x = 0 \\ l\sin(\phi_1) - (b/2)\sin(2\theta_1) + d_1\cos(2\theta_1) - z = 0 \\ b(1+\cos(2\theta_1)) - l\left\{\cos\phi_1 + \cos(-2\theta_1+\phi_1)\right\} = 0 \end{cases} \tag{2}$$

The above system contains three equations in three unknowns (θ_1, d_1, ϕ_1). Hence, it is possible to eliminate two of them and obtain a univariate polynomial involving only one of the variables. In order to simplify the elimination process, the equations are normalized by setting $l = 1$ without any loss of generality. Then, the `Projection` command from the `SIROPA` library of `Maple` was used to obtain the univariate polynomial equation $Q(t) = 0$ in $t = \tan(\phi_1/2)$, where $Q(t)$ is as follows (see [13] for details):

$$4(b+1)^2(x+1)t^4 - 16(b+1)zt^3 + 8\left(b^2-3\right)xt^2 - 16(b-1)zt + 4(b-1)^2(x-1) \tag{3}$$

It has a degree of 4, which indicates that there can be up to 4 real ϕ_1 for a given EE point P. For a feasible value of ϕ_1, a unique combination of (θ_1, d_1) can be computed from the relations in Eq. (2). Thus, the first sub-problem admits up to four solutions for θ_1.

It is noteworthy that the above quartic polynomial degenerates to a cubic form at $(x = -1, z \in \mathbb{R})$ and further to a quadratic form at $(x = -1, z = 0)$. In such scenarios, the number of solutions obtained for t drop to three and two, respectively. Indeed, the missing solutions are formed by $t \to \infty$ (or equivalently $\phi = \pm\pi$), which should be added to the solution set for completeness.

3.2 Second sub-problem

The second sub-problem in inverse kinematics involves computing the angles (θ_2, θ_3) for a given value of θ_1. This sub-problem is confined to the plane π_2 and can be represented graphically as in Fig. 2b. The plane π_2 and the base pivots of the first X-joint in this plane are known once θ_1 is given. Since the point P is also known, the computation of (θ_2, θ_3) is the same as computing the inverse kinematics of a planar 2-X manipulator with offsets. This problem has already been solved in [10], and it is known that there are up to 8 solutions. Thus, combining the two sub-problems, there can be up to 32 (4×8) solutions for the inverse kinematic problem of the 3-X manipulator. The following section presents a numerical example with 32 real solutions for this problem.

3.3 Numerical example

As a numerical illustration, consider the 3-X manipulator with the following geometry: $b = 1$, $l = 2$, and $a = 6$. Note that all the lengths are normalized

w.r.t. b, without any loss of generality. This setting obviates the need to specify the units of points and lengths of the bars. When the EE is positioned at the location $(x, y, z) = (3/2, 1, 3/2)$, 32 real inverse kinematic solutions are obtained as presented in Table 1. The 4 configurations of the first joint and the 8 feasible configurations obtained for each value of θ_1 are presented in Fig. 3.

Table 1: The 32 inverse kinematic solutions for the 3-X manipulator with geometry $b = 1, l = 2, a = 6$ and the EE positioned at $(x, y, z) = (3/2, 1, 3/2)$. All the angular measures are presented in radians.

No.	θ_1	θ_2	θ_3	No.	θ_1	θ_2	θ_3	No.	θ_1	θ_2	θ_3	No.	θ_1	θ_2	θ_3
1		2.81	1.88	9		2.16	2.36	17		2.30	2.19	25		2.00	2.61
2		2.97	-1.62	10		2.36	-1.20	18		2.48	-1.34	26		2.24	-1.03
3		-2.48	1.67	11		-2.22	1.22	19		-2.30	1.37	27		-2.14	1.05
4	2.86	-2.38	-1.82	12	-1.38	-2.04	-2.33	20	-0.68	-2.13	-2.15	28	0.82	-1.91	-2.57
5		-1.13	2.01	13		-1.31	2.50	21		-1.23	2.33	29		-1.42	2.73
6		-0.92	-1.45	14		-1.10	-1.03	22		-1.04	-1.17	30		-1.18	-0.87
7		1.27	1.40	15		1.24	1.01	23		1.21	1.14	31		1.30	0.84
8		1.48	-2.07	16		1.46	-2.53	24		1.41	-2.36	32		1.55	-2.77

Note that these computations do not consider limits on the movement of the joints due to the flat-singularities. In the presence of these limits, i.e., $\theta_i \in \left]-\frac{\pi}{2}, \frac{\pi}{2}\right[$, $i = 1, 2, 3$, only 6 solutions are feasible, as highlighted in Table 1.

4 Singularity analysis

The relation between EE velocity and the joint velocities can be obtained by differentiating the direct kinematic equations in Eq. (1) w.r.t. time. This yields:

$$\begin{bmatrix} \dot{x} \\ \dot{y} \\ \dot{z} \end{bmatrix} = \mathbf{J}_{3\mathrm{x}} \begin{bmatrix} \dot{\theta}_1 \\ \dot{\theta}_2 \\ \dot{\theta}_3 \end{bmatrix} \tag{4}$$

where $\mathbf{J}_{3\mathrm{x}}$ is the Jacobian matrix of the position vector $[x, y, z]^\top$ w.r.t. the joint orientation vector $[\theta_1, \theta_2, \theta_3]^\top$. The singularity condition of the manipulator is obtained from the vanishing of the determinant of $\mathbf{J}_{3\mathrm{x}}$, which, upon clearing the non-zero factors, leads to:

$$\det\left(\mathbf{J}_{3\mathrm{x}}\right) = 0 \implies \sigma_1 \sigma_2 = 0 \tag{5}$$

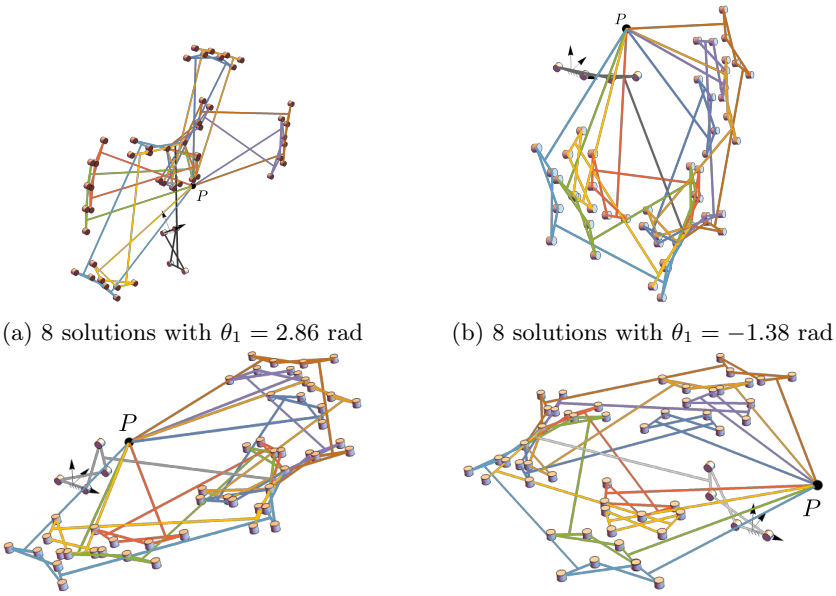

(a) 8 solutions with $\theta_1 = 2.86$ rad

(b) 8 solutions with $\theta_1 = -1.38$ rad

(c) 8 solutions with $\theta_1 = -0.68$ rad

(d) 8 solutions with $\theta_1 = 0.82$ rad

Fig. 3: The 32 inverse kinematic solutions of the manipulator separated into 4 groups, with $b = 1, l = 2, a = 6$ and when the EE is at $(x, y, z) = (3/2, 1, 3/2)$.

where,

$$\begin{aligned}\sigma_1 = &-32a^2 \sin\theta_3 \cos\theta_3 \sqrt{l^2 - b^2\cos^2\theta_2}\sqrt{l^2 - b^2\cos^2\theta_3} \\ &- 4ab^2 \sin(\theta_2 - 2\theta_3)\sqrt{l^2 - b^2\cos^2\theta_3} + 8ab^2 \sin\theta_3 \sqrt{l^2 - b^2\cos^2\theta_2} \\ &+ 8ab^2 \sin(3\theta_3)\sqrt{l^2 - b^2\cos^2\theta_2} + 4ab^2 \sin(\theta_2 + 2\theta_3)\sqrt{l^2 - b^2\cos^2\theta_3} \\ &- 16al^2 \sin\theta_3 \sqrt{l^2 - b^2\cos^2\theta_2} - 8al^2 \sin(\theta_2 + 2\theta_3)\sqrt{l^2 - b^2\cos^2\theta_3} \\ &+ b^4 \sin(\theta_2 - \theta_3) - b^4 \sin(\theta_2 + \theta_3) - b^4 \sin(\theta_2 + 3\theta_3) + b^4 \sin(\theta_2 - 3\theta_3) \\ &- 2b^2l^2 \sin(\theta_2 - \theta_3) + 4b^2l^2 \sin(\theta_2 + \theta_3) + 2b^2l^2 \sin(\theta_2 + 3\theta_3) \\ &+ 8b^2 \sin\theta_3 \cos\theta_3 \sqrt{l^2 - b^2\cos^2\theta_2}\sqrt{l^2 - b^2\cos^2\theta_3} - 4l^4 \sin(\theta_2 + \theta_3)\end{aligned} \tag{6}$$

$$\begin{aligned}\sigma_2 = \left(l^2 - b^2\right)\cos\theta_1 + 2\sqrt{l^2 - b^2\cos^2\theta_1}\Big\{&a\cos(2(\theta_2 + \theta_3)) + a\cos(2\theta_2) + a \\ &+ \cos(2\theta_2 + \theta_3)\sqrt{l^2 - b^2\cos^2\theta_3} + \cos\theta_2\sqrt{l^2 - b^2\cos^2\theta_2}\Big\}\end{aligned} \tag{7}$$

The singularity of the 3-X manipulator occurs when $\sigma_1 = 0$ or $\sigma_2 = 0$. Interestingly, the factor σ_1 is only a function θ_2 and θ_3, while the factor σ_1 involves all three angles. Physically, the vanishing of σ_1 corresponds to the singularity of

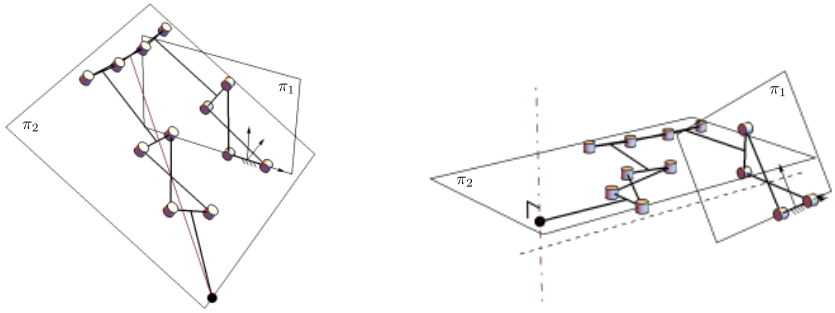

(a) $\sigma_1(\theta_2, \theta_3) = 0$ (b) $\sigma_2(\theta_1, \theta_2, \theta_3) = 0$

Fig. 4: Singular configurations corresponding to $\sigma_1 = 0$ and $\sigma_2 = 0$.

the planar 2-X manipulator in the plane π_2, i.e., when the instantaneous centers of rotation of the two X-joints and the EE point become collinear (see Fig. 4a).

In contrast, at a configuration corresponding to $\sigma_2 = 0$ (see Fig. 4b), the normal to plane π_2 dropped from the EE point intersects with the instantaneous axis of rotation of the first joint. In such a configuration, the velocity produced by the first joint at the EE lies in the plane π_2, just as those produced by the second and third joints. Thus, the EE loses its ability to move out of the plane π_2 at this configuration, making the manipulator singular.

Note that the singularity analysis presented above is valid for any choice of actuation (e.g., ϕ_i, ψ_i) of the X-joints.

5 Workspace

Since the movement of an X-joint is limited by the flat-singularities at $\theta_i = \pm\frac{\pi}{2}$, they should be accounted for while computing the set of reachable joint configurations and the workspace. The joint limits enclose a cube in the joint space, as shown by the golden planes in Fig. 5a. Inside these joint limits, the singularities of the manipulator, i.e., $\sigma_1 = 0, \sigma_2 = 0$, are marked by the grey surfaces. These boundaries are mapped onto the task space using the direct kinematic model in Eq. (1). The resulting contours of the workspace boundaries are presented in Fig. 5b. The workspace is symmetric about the planes $x = 0$ and $y = 0$. However, it is impossible to see the various regions it encompasses.

Hence, further study is conducted by visualizing several cross-sections of the workspace in the following. The workspace is sliced at different values of $x \in [0, 10.5]$. The negative values of x are not considered as the workspace is symmetric about $x = 0$. The resulting cross-sections are displayed in Fig. 6. Important observations from these plots are listed in the following:

– In all sections, a large region with two solutions (green shade) exists. A maximum of six inverse kinematic solutions (orange shade) could be found

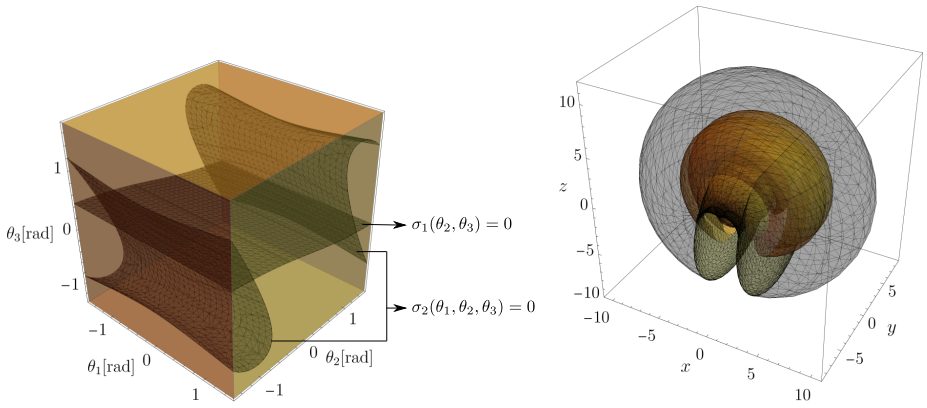

(a) Joint space (b) Workspace

Fig. 5: Joint space and workspace of the 3-X manipulator with geometry $b = 1, l = 2, a = 2$, in the presence of joint limits $\theta_1, \theta_2, \theta_3 \in]-\frac{\pi}{2}, \frac{\pi}{2}[$.

near the origin (section $x = 0$). It reduces to five in the section $x = 1.89$, three in section $x = 2.25$ and two in the remaining sections.
- Around the origin, the reachable workspace is limited to the region $z \in [-3, 10]$ and contains a void in the center. But, beyond $x = 2.25$, the workspace size increases nearly two-fold with a symmetric half along the negative z-axis (see Fig. 5b). As x increases further, the workspace decreases in size until $x \approx 10.5$, and beyond it, the points become unreachable.
- The number of inverse kinematic solutions change by one (resp. two) across a boundary due to joint limits (resp. singularities). However, exceptionally, this change increases to three (resp. four) across joint limits (resp. singularities) in sections $x = 0, 1.89$ due to self-intersections in the respective contours in the workspace.

6 Conclusions

A novel spatial manipulator with three anti-parallelogram (X-joints) arranged in two perpendicular planes was proposed in this work. The inverse kinematic problem was solved by decomposing it into two planar sub-problems. The first sub-problem admits up to four solutions, while the second admits up to eight. Thus, in all, the 3-X manipulator can have up to thirty-two configurations at a given position of the EE. A numerical example was presented to confirm this proposition.

It was found that the singularities of the 3-X manipulator are formed by two conditions, of which at least one of them must be satisfied. The first condition corresponds to the collinearity of the instantaneous centers of rotation of the second and third joints with the EE point. The second condition corresponds to configurations where the velocity induced by the first joint lies in the plane of

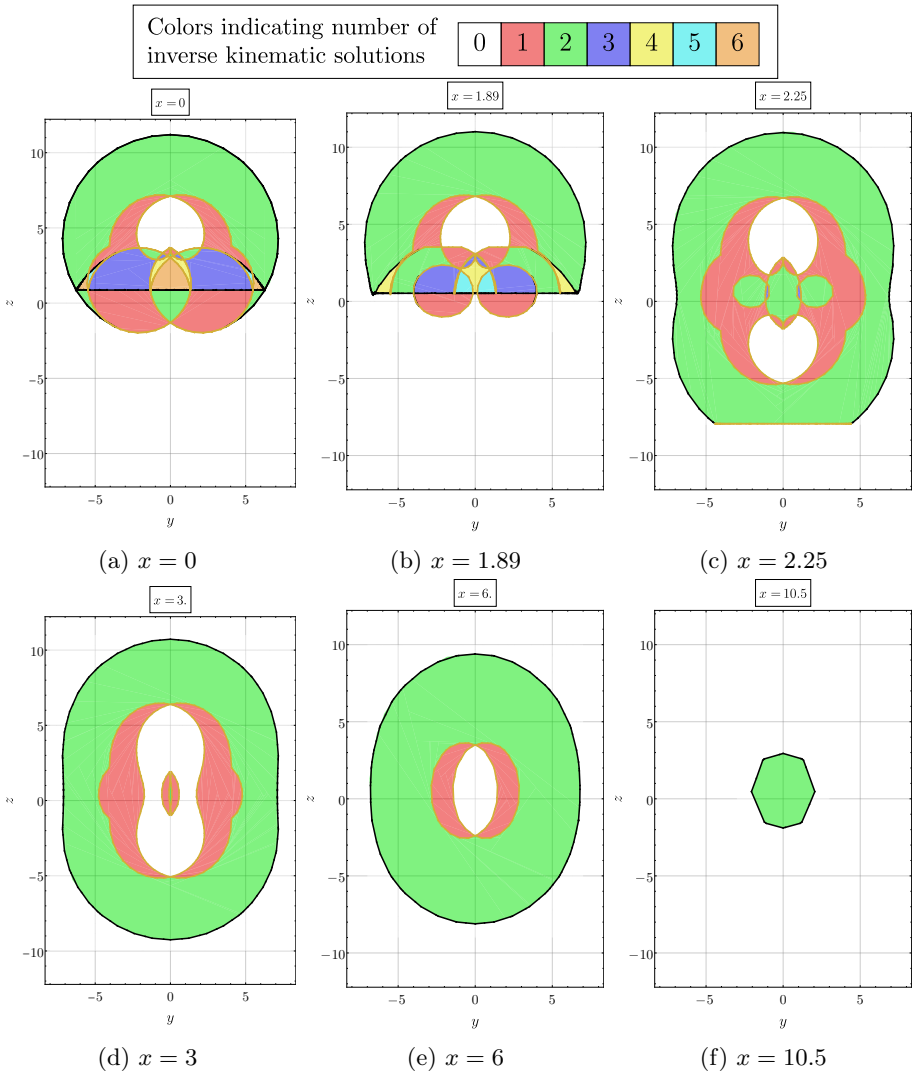

(a) $x = 0$ (b) $x = 1.89$ (c) $x = 2.25$

(d) $x = 3$ (e) $x = 6$ (f) $x = 10.5$

Fig. 6: Cross-sections of the workspace of the 3-X manipulator with geometry $b = 1, l = 2, a = 2$ in the presence of joint limits $\theta_1, \theta_2, \theta_3 \in]-\frac{\pi}{2}, \frac{\pi}{2}[$.

the other two joints. Singular poses corresponding to each of these conditions were presented as illustrations.

Finally, the three-dimensional workspace of the 3-X manipulator was plotted by considering the joint limits due to flat-singularities of each X-joint. Several sections of this workspace were presented to comprehend its interior volume. For the example considered, a maximum of six inverse kinematic solutions exist near the origin and two solutions near the external boundary.

In the future, actuation schemes and instantaneous velocity/force performance of this manipulator will be studied and compared with the existing spatial manipulators composed of revolute joints.

References

1. Siciliano, B., Khatib, O.: Springer Handbook of Robotics. Springer-Verlag, Berlin, Heidelberg (2007)
2. Chen, H.C., Su, W.J., Chen, C.W.: A novel microsurgical robot with double-parallelogram rcm mechanism and back-driven instrument translation. IFAC-PapersOnLine **53**(2), 15940–15945 (2020).
3. Guo, Y., Yin, S., Ren, Y., Zhu, J., Yang, S., Ye, S.: A multilevel calibration technique for an industrial robot with parallelogram mechanism. Precision Engineering **40**, 261–272 (2015).
4. Bakker, D.L., Matsuura, D., Takeda, Y., Herder, J.L.: Design of an Environmentally Interactive Continuum Manipulator. In: Proc. 14th IFToMM World Congress. pp. 327–336. Tapei, Taiwan (2015).
5. Fasquelle, B., Furet, M., Khanna, P., Chablat, D., Chevallereau, C., Wenger, P.: A bio-inspired 3-DOF light-weight manipulator with tensegrity X-joints. In: Proc. 2020 IEEE International Conference on Robotics and Automation. Paris, France (2020).
6. Muralidharan, V., Wenger, P.: Optimal design and comparative study of two antagonistically actuated tensegrity joints. Mech. Mach. Theory **159**, 104249 (2021).
7. Furet, M., Abourachid, A., Böhmer, C., Chummun, V., Chevallereau, C., Cornette, R., De La Bernardie, X., Wenger, P.: Estimating motion between avian vertebrae by contact modeling of joint surfaces. Computer Methods in Biomechanics and Biomedical Engineering **25**(2), 123–131 (2022).
8. Kim, Y.J., Kim, J.I., Jang, W.: Quaternion joint: Dexterous 3-dof joint representing quaternion motion for high-speed safe interaction. In: 2018 IEEE/RSJ International Conference on Intelligent Robots and Systems (IROS). pp. 935–942 (2018).
9. John, I., Mohan, S., and Wenger, P.: Kinetostatic analysis of a spatial cable-actuated variable stiffness joint. J. Mech. Robot. 16(9), 091003 (2024)
10. Wenger, P., Furet, M.: Kinematic analysis of a planar manipulator with anti-parallelogram joints and offsets. In: Lenarčič, J., Siciliano, B. (eds.) ARK 2020. pp. 319–326. Springer International Publishing, Cham (2021)
11. Ghosal, A.: Robotics: fundamental concepts and analysis. OUP (2006)
12. Furet, M., Wenger, P.: Kinetostatic analysis and actuation strategy of a planar tensegrity 2-X manipulator. J. Mech. Robot. **11**(6), 060904 (2019).
13. Chablat, D., Moroz, G., Rouillier, F., Wenger, P.: Using maple to analyse parallel robots. In: Gerhard, J., Kotsireas, I. (eds.) Maple in Mathematics Education and Research. pp. 50–64. Springer International Publishing, Cham (2020)